Nano Energy 129 (2024) 110085

Contents lists available at ScienceDirect

Nano Energy

journal homepage: www.elsevier.com/locate/nanoen

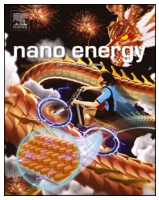

Ultrafast and stable molten salt aluminum organic batteries

Kang Han [a,d], Xinying Qiao [a], Xuanpeng Wang [b,d], Meng Huang [e], Zhenhang Zhong [a], Qi Zhang [a], Chaojiang Niu [c], Jiashen Meng [a,d,*], Liqiang Mai [a,d,*]

[a] State Key Laboratory of Advanced Technology for Materials Synthesis and Processing, School of Materials Science and Engineering, Wuhan University of Technology, Wuhan 430070, China
[b] Department of Physical Science & Technology, School of Science, Wuhan University of Technology, Wuhan 430070, China
[c] School of Materials Science Engineering, Zhengzhou University, Zhengzhou 450001, China
[d] Hubei Longzhong Laboratory, Wuhan University of Technology (Xiangyang Demonstration Zone), Xiangyang, Hubei 441000, China
[e] Sanya Science and Education Innovation Park of Wuhan University of Technology, Sanya 572000, China

ARTICLE INFO

Keywords:
Aluminum Ion Batteries
Molten Salt Electrolyte
Aluminum Storage Mechanism
π-π Conjugated Regulation
Organic Cathode

ABSTRACT

Aluminum-organic batteries (AIBs) have gained significant popularity for large-scale energy storage due to their abundance of aluminum reserves, cost-effectiveness, and environmental friendliness. However, the current aluminum-organic batteries primarily relied on ionic liquid electrolytes suffer from slow reaction kinetics and limited cycle life. Herein, we report a novel and efficient aluminum-organic battery that addresses these limitations by utilizing a molten salt electrolyte and designing a strongly interacting organic cathode. By enhancing π-π stacking interactions, we induced a transition in commercial PTCDA (Perylene-3,4,9,10-tetracarboxylic dianhydride) molecules from the β-phase to the highly interactive α-phase, known as PA450. This transformation not only stabilizes the structure of the PA450 electrode, preventing dissolution in the molten salt electrolyte, but also significantly improves electron conductivity. The Al||PA450 molten salt battery demonstrates exceptional electrochemical performance, exhibiting a high reversible capacity of 135 mAh g^{-1} and outstanding cyclability for up to 2000 cycles at 10 A g^{-1}. Additionally, the structural rearrangement and ion transport properties induced by the co-intercalation of Al^{3+} and $AlCl_2^+$ were studied are investigated. This work provides deep insights into the unique characteristics of organic materials for ultrafast energy storage in molten salt electrolytes.

1. Introduction

In response to the urgent challenges posed by climate change and the energy crisis, grid-scale energy storage systems (ESS) are increasingly recognized as essential components for advancing sustainable energy supply in the market landscape [1–4]. Although lithium-ion batteries (LIBs) currently dominate the electrochemical sector of the ESS market, their widespread adoption is hindered by the scarcity and associated high costs of lithium resources [5–7]. This limitation is exacerbated by the burgeoning demand within the electric vehicle sector. Consequently, there is a compelling need to explore viable alternatives to LIBs. Rechargeable aluminum batteries (RABs) have emerged as a promising contender due to their cost-effectiveness, inherent safety when exposed to air, and the abundant presence of aluminum in the Earth's crust (comprising 8.1 wt%) [8–12]. Furthermore, the aluminum metal anode shows a notably high theoretical capacity of 8040 mAh cm^{-3}, making a significant contribution to the advancement of high-capacity RABs [13]. However, the exploration of RABs remains in its nascent stages, primarily hindered by the need to develop positive electrode materials characterized by high capacity, rapid kinetics, and long-term cycling stability [12].

For the Al(III) species formed during cycling, the charge carriers in cathode materials include Al^{3+}, $AlCl^{2+}$, $AlCl_2^+$) [8,11,14–16] or as anions ($AlCl_4^-$ and $Al_2Cl_7^-$) [17,18]. However, contrary to the initial motivation for three-electron storage, only a few examples of Al^{3+} storage have been reported in specific metal oxides [11,14,16] and sulfides [19–22]. This limitation primarily arises from the strong Coulombic interactions between Al^{3+} and the host materials, leading to sluggish diffusion kinetics at high current densities [23]. Instead, Al^{3+} converts oxides and sulfides into Al_2O_3 and Al_2S_3 on the surface [24], which is undesirable for subsequent oxidization. As a result, most cathode materials identified in AIBs to date function by storing monovalent aluminum complex

* Corresponding authors at: State Key Laboratory of Advanced Technology for Materials Synthesis and Processing, School of Materials Science and Engineering, Wuhan University of Technology, Wuhan 430070, China.
E-mail addresses: jsmeng@whut.edu.cn (J. Meng), mlq518@whut.edu.cn (L. Mai).

https://doi.org/10.1016/j.nanoen.2024.110085
Received 20 March 2024; Received in revised form 23 July 2024; Accepted 2 August 2024
Available online 3 August 2024

ions, such as $AlCl_4^-$ and $AlCl_2^+$. However, this monovalent ion storage mechanism greatly reduces the charge density of the whole system. These materials include carbon materials [18,25,26], metal sulfides [27,28], and metal selenides [29,30]. Regarding carbon materials, various graphene-based materials have been explored since the original report by Lin et al. [31], revealing the reversible storage of $AlCl_4^-$ in graphite. However, when considering energy density, the utilization of $AlCl_4^-$ in the electrolyte reaction is not optimal due to the significant constraint it poses on battery energy density progress, primarily because of the considerable quantity of electrolyte required.

In recent years, the selection of cathode materials for AIBs has been expanded to organic molecules, such as carbonyl compounds [8,32,33], nitrile compounds [15], conductive polymers [34], and covalent organic polymers [35,36]. For example, Wu et al. constructed a polythiophene cathode (PT) with adaptive restructuring capability to achieve ultra-long stability [37]. Such cathode can spontaneously adjust their molecular aggregation mode during battery cycling, reducing the electrostatic repulsion between $AlCl_4^-$ during charging and suppressing electrode structure deformation caused by large electrostatic repulsion. Yamauchi et al. reported an aluminum-organic battery based on a dual-site synergistic mechanism of PYTQ [38]. When nitrogen atoms were introduced to the carbonyl β position, C═N could stably bind with the large aluminum-ion group in coordination with C═O. However, despite the encouraging progress in Al-organic battery research, most organic materials still face challenges in effectively harnessing the three-electron transfer properties of Al^{3+} for efficient storage. Additionally, organic small molecules still face issues such as significant dissolution and poor rate performance in ionic liquids. By successfully replacing the commonly used ionic liquids with a low-cost inorganic chloride molten electrolyte, a highly secure, ultra-low-cost, and fast-charging molten salt aluminum battery has been reported by our research team [39]. Excitingly, the rapid dissociation kinetics of Al^{3+} in the molten salt electrolyte and at an elevated temperature offer promising opportunities for harnessing the three-electron transfer properties that organic materials often struggle to exhibit in ionic liquids. However, it is unfortunate that there is currently limited research on the energy storage properties of organic cathodes in molten salt electrolytes, and further investigation is needed to understand their reaction mechanisms.

In this study, we develop an economically efficient, high-rate, and stable aluminum-organic battery through the concurrent utilization of a molten salt electrolyte and the design of a strongly π-π stacking interactions organic cathode. The heightened π-π stacking interactions not only facilitates electron transport between molecular layers but also confers additional negative charges to the terminal oxygen, thereby significantly enhancing ion diffusion kinetics. The incorporation of molten salt electrolytes further enhances reaction kinetics and effectively prevents material dissolution. Moreover, by integrating density-functional theory (DFT) calculations with experimental analysis, our study reveals that the Al||PA450 molten salt battery is capable of utilizing both $AlCl_2^+$ and Al^{3+} ions. This dual-ion utilization enhances the multi-electron storage characteristics of the AlBs, resulting in a reversible specific capacity of 135 mAh g^{-1} at 1 A g^{-1}. Even at 10 A g^{-1}, it maintains a significant specific capacity of 90 mAh g^{-1} over 2000 cycles. This design principle and research findings not only expand the application of organic cathode in AlBs, but also lay a solid foundation for the future development of high-performance aluminum-organic batteries.

2. Results and discussion

2.1. Construction of strongly interacting organic cathodes

The control of the phases and conjugated stacking structures of the PTCDA (Perylene-3,4,9,10-tetracarboxylic dianhydride) is achieved through a simple one-step annealing process. Specifically, commercial PTCDA is utilized as the initial control group (designated as PA), and subjected to vacuum annealing at 450 and 650 ℃ for 2 hours, resulting in the formation of two samples labeled as PA450 and PA650, respectively. Thermal gravimetric analysis (TGA) and scanning electron microscopy (SEM) images clearly indicate that the PA450 sample shows minimal thermal loss, but exhibits a certain degree of recrystallization. Conversely, the PA650 sample undergoes noticeable thermal decomposition and experiences morphological transformation (Fig. S1 and S2). XRD analysis was employed to reveal the structural differences of PTCDA before and after heat treatment. According to previous reports, PA450 and PA correspond well to the α and β phases of PTCDA [40,41], respectively, while PA650 no longer possesses a crystalline structure due to extensive thermal decomposition. The front view of the unit cells of PA450 and PA (Fig. 1b-c) and their corresponding stereograms show that they have similar arrangements along the a-axis, but slightly differ in layer stacking and molecular orientation (Fig. S3). Compared to β-PTCDA, in α-PTCDA, each atom in a molecule is directly above the corresponding atom in the molecule below, with a minimal distance of 3.21 Å (β-PTCDA, 3.25 Å) between two adjacent molecules. This regular planar stacking and close intermolecular spacing enhance extensive π orbital overlap, making the electrons delocalized in the direction perpendicular to the molecular plane, resulting in higher electron mobility and better electron transport properties. Additionally, heat treatment further increases the structural stability of PA450. The shift towards higher angles of the (102) diffraction peak and the appearance of the (110) diffraction peak at 25.6° further confirm the enhancement of these π-π stacking interactions, consistent with those reported for other perylene diimide derivatives (Fig. 1d) [40,42,43]. UV–vis spectra provide additional evidence of increased π-π stacking in PA450, with a red shift (~60 nm) indicating an enlarged conjugate system (Fig. 1e) [42]. Furthermore, optical images of various samples (Fig. S4) reveal a color shift from bright red powder to dark brown and black upon different thermal treatments, suggesting enhanced conjugated structures and conductivity due to changes in light absorption properties. The voltammetric characteristics curve and the electrochemical impedance results also provide substantial evidence for the improved electrical conductivity of the PA sample after undergoing moderate thermal treatment (Fig. S5 a-b). The infrared spectra reveal a high degree of similarity between the functional groups of PA450 and the original PA (Fig. S6), indicating that annealing at 450°C did not change the intrinsic structure and molecular environment of PTCDA, except for enhancing its conductivity [44]. Conversely, PA650 exhibits severe damage to its functional groups, consistent with the findings from XRD analysis. The XPS spectra showed that all three types of samples only exhibited C and O signal peaks, with a notable reduction in the intensity of the O1s peak for PA650, indicating a violent decomposition and transformation into carbon material after annealing at 650°C (Fig. 1f). Furthermore, in the C 1 s and O1s high-resolution spectra (Fig. 1g), a decrease in the intensity of the C═O bond and an enhancement in the C-O single bond in PA450 was observed. Additionally, there is an increase in the O1s binding energy. This rise is mainly due to enhanced π-π conjugation, which increases electron density on carbon and alters electron deficiency on oxygen, thereby raising overall oxygen binding energy [45,46]. To delve deeper into the electronic delocalization characteristics and the variations in internal bonding interactions among different crystalline phases of PTCDA, we further employed the Localized Orbital Locator Integrated Pi Over Plane (LOL-π) and Reduced Density Gradient (RDG) analysis methods [47–49]. The LOL-π results highlight prominent electronic delocalization on the benzene rings of PTCDA, further suggesting that π electrons can move relatively freely throughout the entire molecule, thus exhibiting favorable electron transport properties (Fig. 1i). The RDG analysis compared the α-phase of PA450 with PA (Fig. 1j-k), highlighting more continuous and robust π-π interactions in areas marked by weak van der Waals forces in PA450. This is graphically evident, offering a clear visualization of the conjugation strength variations in different phase structures.

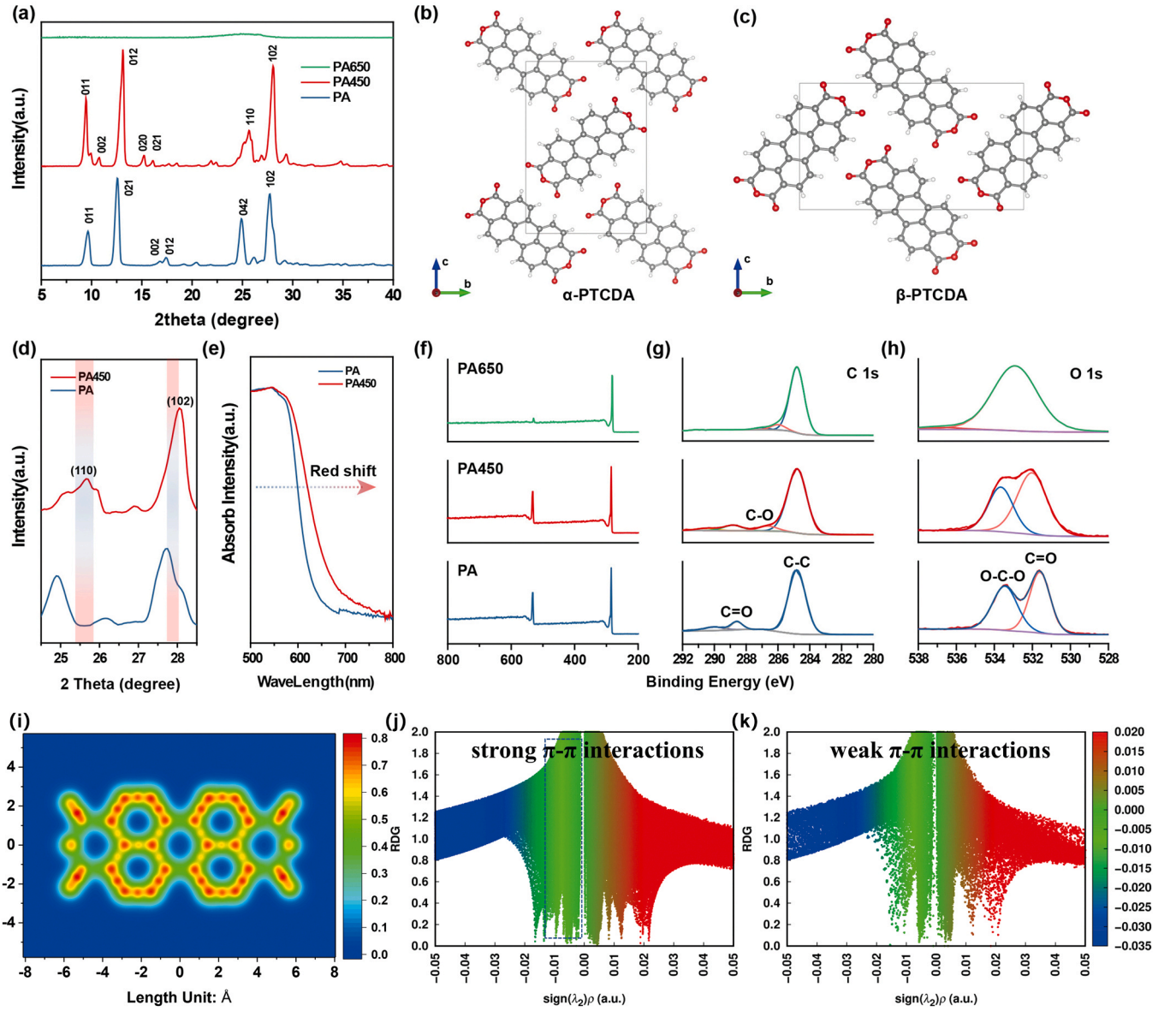

Fig. 1. Structure characterizations of the PA, PA450 and PA600 samples. (a) XRD patterns of PA, PA450 and PA650 samples. (b, c) Atomic structures of PA450 and PA. (d) Local XRD magnification of PA450 and PA. (e) UV–vis spectra of the PA and PA450. (f-h) XPS spectrum of PA, PA450 and PA650 samples, (f) wide spectrum (g) High-resolution C1s spectrum (h) High-resolution O1s spectrum. (i) Localized orbital locator integrated Pi Over Plane (LOL-π) analysis of PTCDA. (j-k) Reduced density gradient analysis of PA450(α phase, j) and PA (β phase, k).

2.2. Electrochemical performance evaluation

To evaluate the electrochemical performance of the three samples in AIBs, cells are assembled using Al foil as anode in a Swagelok-type configuration and tested at 120 °C. Cyclic Voltammetry (CV) curves show that PA450 and PA samples exhibit similar redox peaks, but PA450 displays lower electrochemical polarization (~40 mV). In contrast, PA650 no longer displays significant electrochemical activity (Fig. 2a). Subsequently, the electrochemical performance of PA450 was compared in ionic liquid and molten salt electrolytes to highlight the notable role of molten salt electrolytes. Notably, in both of these electrolytes, a noticeable weakening of the plateau and transition during the initial cycles was observed. Nevertheless, PA450 exhibited much better cycling stability in the molten salt electrolyte, while experiencing rapid capacity loss observed in the ionic liquid. Specially, in the molten salt electrolyte, the PA450 sample achieves swift stabilization after just 10 cycles, maintaining a reversible specific capacity of 100 mAh g^{-1} during subsequent cycling (Fig. 2b). The gradual capacity fade observed during the initial 10 cycles may be attributed to the loss of active material due to partial dissolution of PA450 in the molten salt electrolyte or to irreversible phase transitions caused by the intercalation of Al^{3+}. Conversely, in the ionic liquid, aluminum storage activity in PA450 was nearly lost after 10 cycles (Fig. 2c). The dissolution experiments showed that PA450 maintained a low solubility in the molten salt electrolyte even after 1 h, whereas significant material dissolution discoloration was observed in the ionic liquid after only 1 min (Fig. S7). Moreover, the PA450 electrode also exhibits outstanding rate performance in the molten salt electrolyte. High specific capacities of 140, 134, 120, and 102 mAh g^{-1} are obtained at 1, 3, 5, and 10 A g^{-1}, respectively. Even when returned to 1 A g^{-1}, a specific capacity of 134 mAh g^{-1} is maintained, corresponding to 96 % capacity retention (Fig. 2d). At the same current densities, the PA450 electrode in the molten salt electrolyte exhibits reversible specific capacities that are approximately twice as high as those in the ionic liquid (Fig. 2e). The extracted voltage-time curves clearly display the exceptional ultrafast reaction kinetics of the Al||PA450 molten salt battery (Fig. 2f). It is evident that, the battery can

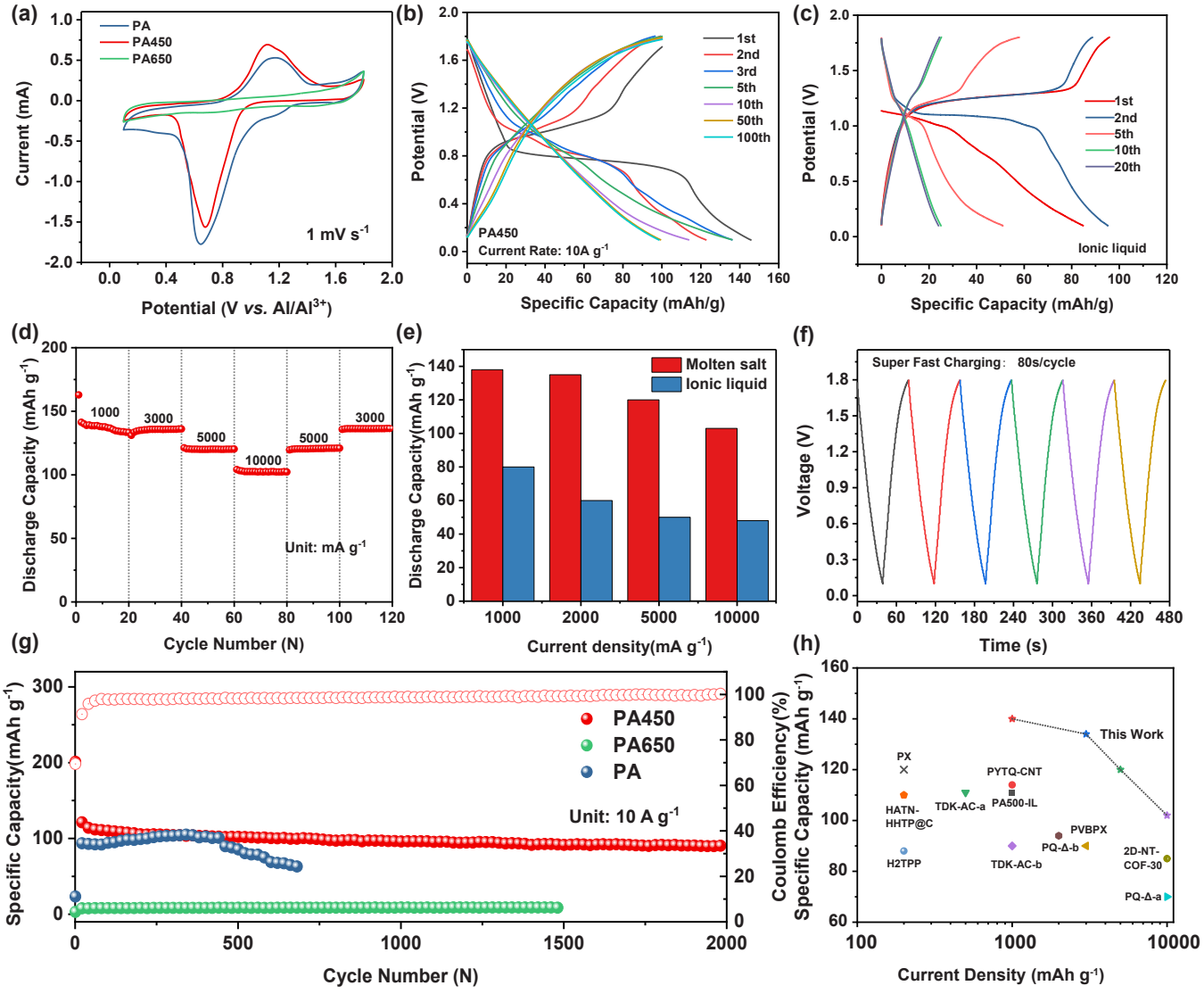

Fig. 2. Electrochemical measurements of the PA, PA450 and PA650 electrodes. (a) Typical CV curves of PA, PA450 and PA650 electrodes based on molten salt electrolyte. (b) Galvanostatic charge/discharge (GCD) curve of PA450 at molten salt electrolyte. (c) GCD curve of PA450 at ionic liquid electrolyte. (d) Rate performance of Al||PA450 molten salt cells. (e) Comparison of PA450 performance between molten salt electrolyte and ionic liquid electrolyte at different current densities (f) Voltage-time curve of PA450 at 10 A g^{-1} (g)Long-term cycling stability of PA, PA450 and PA650 electrodes in molten salt cells under 10 A g^{-1}. (h) Comparative performance chart of typical organic cathodes.

complete a full charge and discharge cycle in just 80 seconds at 10 A g^{-1}, which meets the demand for fast energy storage. The long-term cycling stability test at 10 A g^{-1} indicates that the PA450 maintains a specific capacity of 90 mAh g^{-1} even after 2000 cycles, while the PA exhibits only 60 mAh g^{-1} after 700 cycles. Additionally, the PA650 does not possess Al storage ability at such high current density (Fig. 2g). To our best knowledge, this represents the first report of a fast-charging aluminum-organic battery based on a molten salt electrolyte. The Al||PA450 molten salt cell exhibits exceptional rate capability and cycling performance far surpassing most previously reported AIB cathodes [8,15,37,38,50–53] (Fig. 2h).

To gain a deeper understanding of the charge storage process of PA450 in molten salt electrolytes, we further analyzed the diffusion dynamics based on characteristic CV curves recorded at scan rates between 2 and 10 mV/s (Fig. S8a). The relationship between the peak current and the scan rate in the CV curves can be described by the equation $i = av^b$. For an ideal Faradaic process controlled by semi-infinite linear diffusion, the value of b is 0.5, while for surface charge storage processes, b approaches 1. Calculation of b values from the redox peaks resulted in 0.66 and 0.65, respectively (Fig. S8b), suggesting a predominance of diffusion-controlled Faradaic processes in PA450. Further quantitative differentiation between diffusion and surface capacitive contributions was performed using the formula $i(V)/v^{(1/2)} = k1 * v^{(1/2)} + k2$. At a scan rate of 2 mV/s, the pseudocapacitive contribution of PA450 in the molten salt electrolyte accounted for 41 % of the total capacity (Fig. S8c). When the scan rate was increased to 10 mV/s, the capacitive contribution rose to 77 % (Fig. S8c-d). This indicates that at low current densities, PA450 primarily relies on Faradaic diffusion reactions, while at higher current conditions, charge storage is predominantly governed by surface capacitance, significantly enhancing the rapid storage and long-term cycling stability of PA450 in molten salt electrolytes.

Furthermore, as depicted in the Ragone plot (Fig. S9), the developed Al||PA450 molten salt cell exhibits significant advantages in terms of energy/power density compared to traditional supercapacitors, commercial capacitors, and primary lithium batteries [54]. The exceptional rate and cycle performance of Al||PA450 molten salt cells can be attributed to several key factors. First, the facile breaking of Al-Cl-Al

bonds in molten salt electrolyte, providing faster charge transfer kinetics for its reactions. Second, the PA450 sample possesses a multi-electron system with abundant delocalized large π bonds, which facilitates electron transfer. Lastly, the molten salt electrolyte effectively mitigates the challenge of facile dissolution of organic small molecules, which is a common issue with ionic liquids.

2.3. Reaction mechanism identification

To investigate the interfacial structural components of the PA450 electrode in the molten salt electrolyte, we conducted Time-of-Flight Secondary Ion Mass Spectrometry (TOF-SIMS) measurements on electrodes that were fully charged and discharged. The schematic representation of the TOF-SIMS is depicted in Fig. 3a. In this setup, a pulsed bismuth (Bi) ion beam is used to induce desorption or ionization of atoms and molecular groups on the solid surface, acting as a positive ion source. Subsequently, the resulting secondary ions are accelerated into the mass spectrometer and separated based on their time of flight from the sample to the detector [53,55]. During the analysis of the mass spectrum of the surface layer, the ion beam was utilized to ablate the surface material layer, allowing for the construction of a depth distribution in conjunction with electrode profile depth analysis (Fig. 3b).

The analysis of 2D chemical ion images obtained from the PA450 electrode in both fully discharged and charged states revealed the presence of five distinct secondary ions: Al+, $AlCl_2$+, AlCl+, Cl+, and Al_2Cl_3+ (Fig. S10). It is worth mentioning that in the TOF-SIMS test, we only observed the presence of weak $AlCl_4$+ and Al_2Cl_7+ components in both fully discharged and charged states, which indicates that unlike the typical graphite $AlCl_4^-$ intercalation reaction, the energy storage of PA450 in molten salt electrolytes is likely not dominated by $AlCl_4^-$ or $Al_2Cl_7^-$ (Fig. S11). Notably, the 3D depth-rendered images (Fig. 3c and 3d) demonstrated that among these cations, only Al+ and $AlCl_2$+

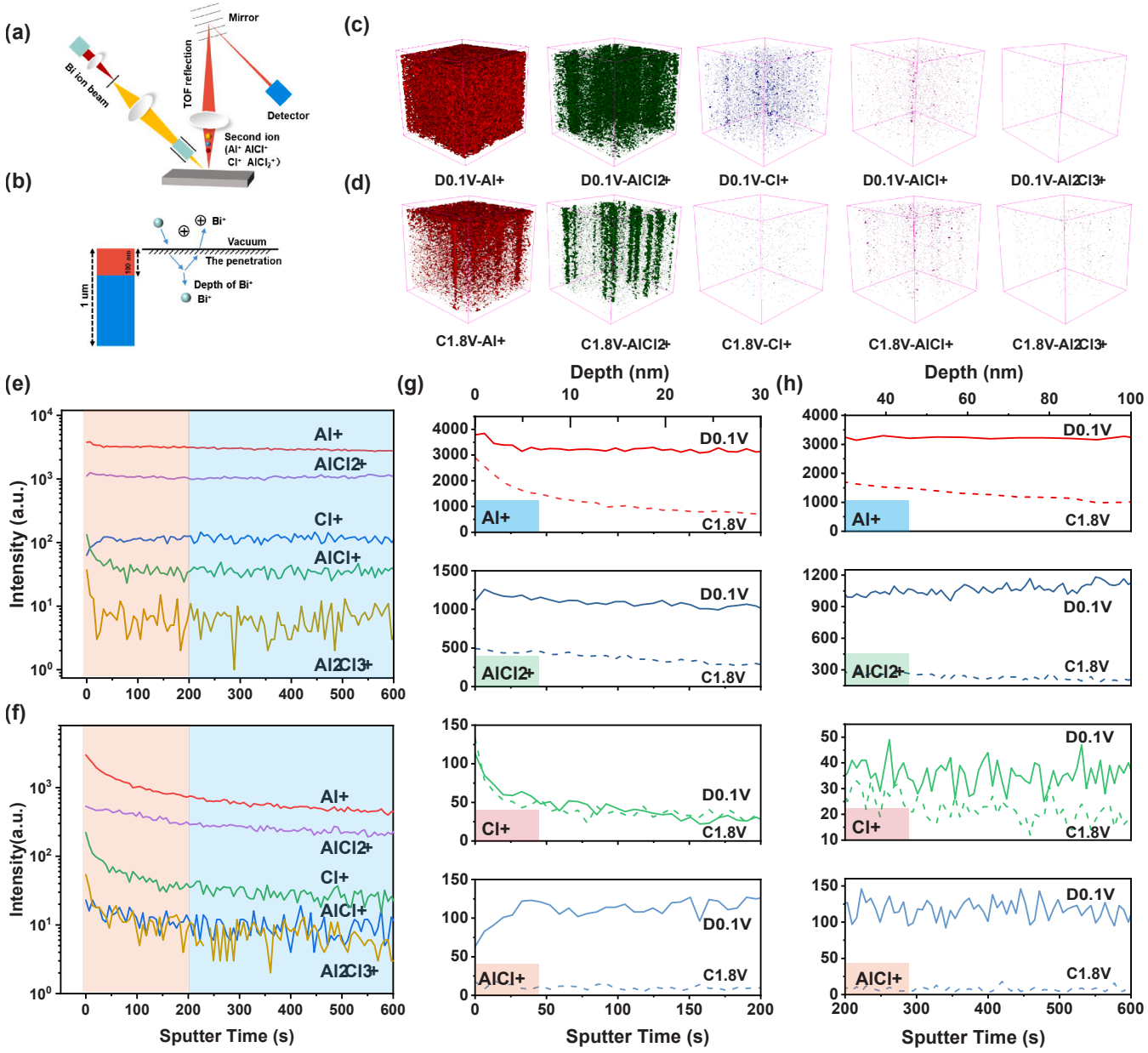

Fig. 3. TOF–SIMS of PA450 electrode at fully discharged and charged states. (a) The schematic diagram of TOF–SIMS. (b) the diagram of deep sputtering. (c, d) 3D images of the sputtered volume corresponding to the depth profiles at discharge-0.1 V and charge-1.8 V. (e-f) depth profiles at discharge-0.1 V (e) and charge-1.8 V (f). (g, h) the magnified TOF–SIMS depth curves at 0–30 nm (g) and 30–100 nm (h).

exhibited more pronounced content distributions. The depth-distribution curves of the PA450 electrodes further indicated that the intensities of the various cationic constituents were significantly higher during discharge to 0.1 V (Fig. 3e) compared to charging at 1.8 V (Fig. 3f) . Moreover, the intensity ratios of the four different ions (Al+, $AlCl_2$+, AlCl+, and Cl+) at depths of 0–30 nm (Fig. 3g) and 30–100 nm (Fig. 3h) illustrated that cations displayed a substantial decrease in the depth range of 0–30 nm, maintaining stability in the 30–100 nm region. During both charging and discharging states, the predominant cationic forms are Al+ and $AlCl_2$+, with no spectral signals of $AlCl_4$+ or Al_2Cl_7+ observed at their interfaces. This indicates that the energy storage mechanism in PA450 may involve co-intercalation of Al^{3+} and $AlCl_2^+$. Furthermore, the intensity ratios of the Al+, AlCl+, and $AlCl_2$+ at different depths were also compared (Fig. S12). During discharge to 0.1 V, the distribution of Al+ and $AlCl_2$+ prevailed, with their contents remaining relatively constant. This indicates that Al^{3+} and $AlCl_2^+$ are deeply integrated within PA450. In contrast, during full charging at 1.8 V, the content of Al+ decreased with increasing depth, suggesting that Al^{3+} undergoes de-intercalation or transformation into $Al_xCl_y^+$.

Furthermore, *in-situ* XRD analysis was employed to unveil the distinctions in phase transitions and stability between the initial PA and PA450 in the molten salt electrolyte. It was evident that a distinct signal peak persisted for PA450 even after three cycles (Fig. 4a), whereas the peak vanished during the first cycle of discharge for PA (Fig. 4b). This observation highlights the superior structural stability of PA450, which is attributed to its robust π-π interactions and increased thermal stability after undergoing heat treatment. Simultaneously, the diffraction peak of the (102) plane, located at 2θ=27.2°, progressively shifted to a lower angle during the initial discharge process (Fig. S13). This shift suggests structural rearrangement caused by the co-insertion of Al^{3+} and $AlCl_2^+$. In the *ex-situ* IR spectroscopy (Fig. 4c), noticeable reversible changes were observed in the C═O stretching vibration at 1820 cm^{-1} and the C═C stretching vibration at 1650 cm^{-1} during the charging and discharging processes. Furthermore, in the Raman spectra, the C-H in-plane bending vibration, situated at 1298 cm^{-1}, gradually shifted to lower wavenumbers (Fig. S14). All these alterations in peak positions and intensities are attributed to changes in the electron cloud density of PA450 and the rearrangement of the crystal structure during the electrochemical reaction.

Additionally, *ex-situ* X-ray photoelectron spectroscopy (XPS) was employed to investigate the interaction between the functional groups of PA450 and charge carrier ions at various charge-discharge potentials. For the initial charge-discharge process of PA450, six representative potentials were selected for the study (Fig. 4d), and all signal peaks were charge-corrected based on C-C at 284.8 eV as the reference. In the C1s spectrum, a noticeable increase in the interaction of the C═C within the

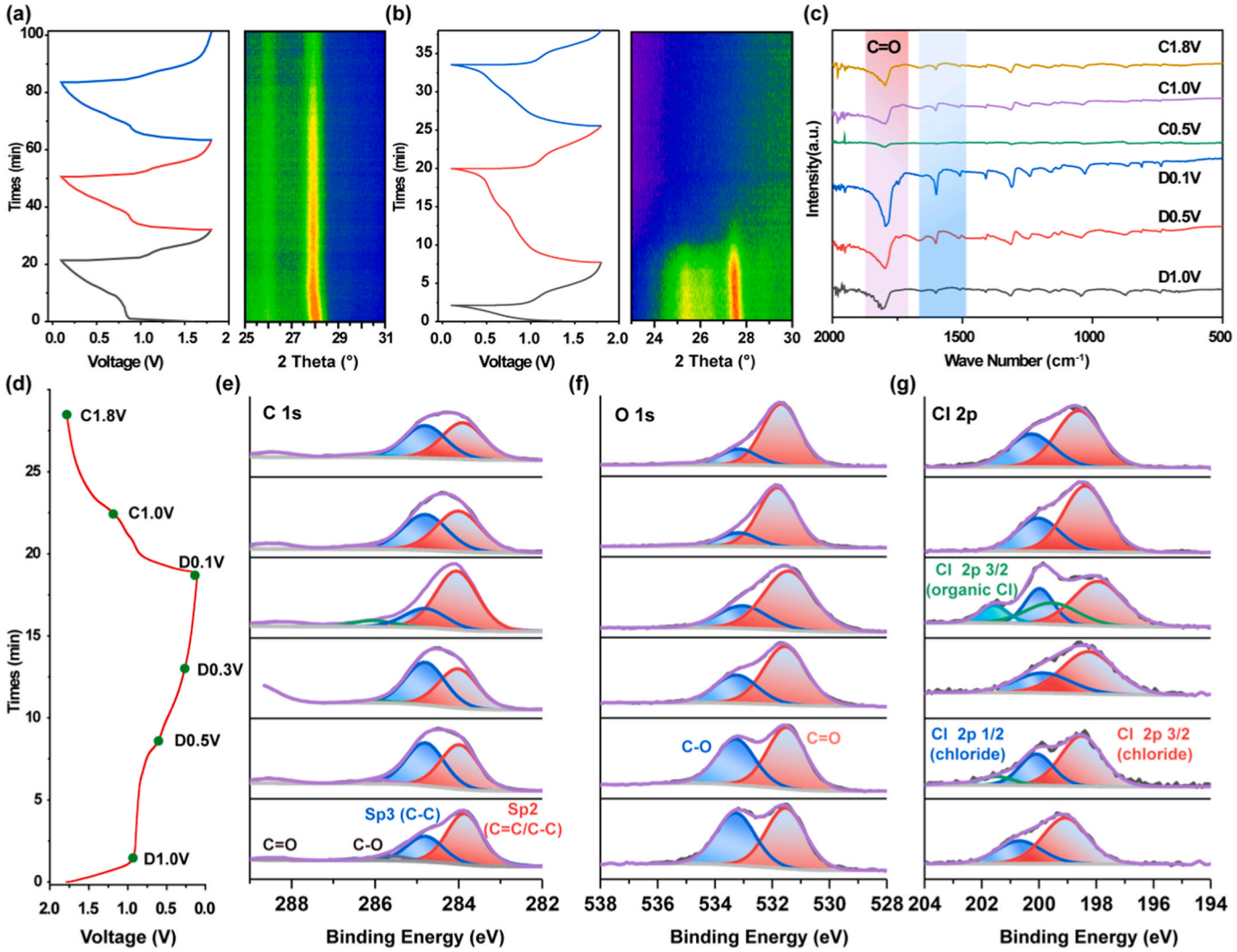

Fig. 4. Characterizations and analysis of redox mechanism of PA450 in molten salt cells. (a, b) In-situ XRD structural evolution of PA450(a) and PA (b) during the first three charge-discharge cycles. (c) Ex-situ Raman spectra at different potentials. (d-g) The voltage-time curve for the first cycle(d), and XPS curves of C 1s(e), O 1s(f), Cl 2p(g).

aromatic benzene ring was observed, while the interaction of the C-C was weakened (Fig. 4e). This finding is consistent with the trends observed in aforementioned Raman and FTIR peak changes, indicating that ion insertion during the electrochemical transition process triggers some structural reorganization. In the O1s spectrum, the C═O intensity decreases only during discharge, followed by an increase during charging, while the binding energy remains unchanged (Fig. 4f). This suggests the occurrence of an enolization reaction between C═O and $AlCl_2^+$, as reported in previous studies [42]. The split Al XPS spectra show a decrease in binding energy from 74.6 eV to 74.1 eV when discharged to 0.5 V and 0.1 V, respectively (Fig. S15a), which is significantly lower than the binding energy of Al in standard ternary molten salt electrolytes (76.2 eV) and $AlCl_3$ (75.7 eV) (Fig. S15b). The decrease in binding energy indicates a reduction in the Al-Cl bonding ratio in each component, as the electron-withdrawing of highly electronegative Cl significantly increases the positive charge of Al when bonded to it. The more Cl atoms bonded to Al, the higher the positive charge on Al, resulting in a higher binding energy. Raman spectroscopy indicates the presence of $AlCl_4^-$ clusters in the ternary molten salt electrolyte, thus exhibiting the highest binding energy (Fig. S16). The binding energy at 74.1 eV is consistent with that of Al in Al_2O_3, suggesting complete removal of Cl upon discharge to 0.1 V, corresponding to the presence of Al^{3+}. When discharged to 0.5 V, the binding energy lies between that of Al^{3+} and $AlCl_3$, and combined with the TOF-SIMS compositional analysis, it can be inferred that this corresponds to the presence of $AlCl_2^+$. In the fully discharged state, organic chlorine signals are detected in the Cl 2p spectrum (Fig. 4g), further confirming the embedding of low-order Al^{3+}/$AlCl_2^+$ into the aromatic structure of PA450, replacing some of the H in the aromatic hydrocarbons. These findings align with the conclusions drawn from the C1s spectrum and FTIR data.

It is important to clarify that the embedding of Al^{3+} in PA450 may only occur in the initial cycles. This is because in the Al XPS spectra after 20 cycles, even in the fully discharged state, only the $AlCl_2^+$ signal is observed on the PA450 surface, without showing the characteristic binding energy of Al^{3+}(Fig. S17). The TOF-SIMS tests of the fully discharged state after 100 cycles also observed that the surface $AlCl_2$+ component was higher than Al+ (Fig. S18), further indicating that the insertion of Al^{3+} likely occurs only in the initial cycles, with the subsequent cycles being predominantly governed by the insertion/adsorption of $AlCl_2^+$. Similarly, both Cl XPS and ex situ Raman results at different potentials exhibit no significant changes (Fig. S19 and Fig. S20c). This may be due to the strong Coulomb interaction between Al^{3+} with high surface charge density and the carbonyl group in PA450 when Al^{3+} is embedded in the crystal structure of PA450. This interaction may cause irreversible damage to the lattice structure of PA450, leading to the transformation of PA450 from crystalline to amorphous phase. The lattice reconstruction caused by Al^{3+} embedding is irreversible, which also explains why the charge-discharge curve platform disappears and the capacitance-based energy storage characteristics change after several cycles. In addition, periodic changes of C═C and C═O can still be observed in the C and O spectra after 20 cycles, corresponding to the enolization reaction of $AlCl_2^+$ with C═O (Fig. S20a-b). Nevertheless, in subsequent cycles, PA450 still exhibits ultra-stable cycling stability and high rate performance. Raman and infrared spectra of PA450 electrodes cycled 50, 100, 500, and 1000 times were further used to verify their structural and electrochemical stability during long-term cycling (Fig. S21). The results show that the overall structural features and signal intensity of PA450 remain basically unchanged during long-term cycling. This may be due to the fact that the interface adsorption based on $AlCl_2^+$ dominates in the ultra-high current charge and discharge process, thus showing ultra-high rate performance.

The representative discharge curve of the Al||PA450 battery further confirms the reliability of Al storage through the insertion of Al^{3+} and $AlCl_2^+$ in the molten salt electrolyte. The discharge process involves approximately four electron transfers, occurring in two stages: the first stage involving one electron transfers, while the second stage involving three electrons transfers (Fig. 5a). This staged electron transfer feature coincides with the proposed multi-stage coupling mechanism based on $AlCl_2^+$ and Al^{3+} co-embedding. Density Functional Theory (DFT) calculations were also employed to determine the binding energies between PA450 and different aluminum-coordinating ions (Al^{3+}, $AlCl_2^+$, $AlCl^{2+}$, $AlCl_4^-$ and $Al_2Cl_7^-$). Binding energy serve as a metric for both the thermodynamic stability of the reaction process and revealing the preferred charge carriers in electrolyte electrochemical reactions [15]. The research findings indicate that the binding energies of Al^{3+}, $AlCl_2^+$, $AlCl^{2+}$, $AlCl_4^-$, and $Al_2Cl_7^-$ with PA450 are −4.26 eV, −3.74 eV, −3.71 eV, −2.05 eV, and −3.50 eV, respectively (Fig. 5b). This provides substantial evidence that aluminum-coordinating cations serve as the preferred charge carriers for the C═O. Although the binding energy of $AlCl^{2+}$ is similar to that of $AlCl_2^+$, the absence of a distinct $AlCl_2^+$ signal in the TOF-SIMS test suggests the presence of competitive effects during dissociation, indicating that the $AlCl^{2+}$ component does not dominantly participate in the dissociation process of the high-chain segment $Al_nCl_{(3n+1)}^-$. Furthermore, an assessment of the highest occupied molecular orbital (HOMO) and lowest unoccupied molecular orbital (LUMO) energy levels in PA450 after the insertion of various aluminum-coordinating ions provides additional confirmation of the multi-stage co-insertion mechanism of $AlCl_2^+$ and Al^{3+} in the molten salt electrolyte. Typically, the HOMO-LUMO gap partially reflects the material's stability, with a higher Eg (energy gap) value indicating greater stability [56,57]. The HOMO-LUMO gap values for the five aluminum-coordinating ions (Al^{3+}, $AlCl_2^+$, $AlCl^{2+}$, $AlCl_4^-$, and $Al_2Cl_7^-$) bound to PA450 are 1.36 eV, 1.37 eV, 1.45 eV, 1.10 eV, and 0.12 eV, respectively (Fig. 5c). It is evident that the PA-Al^{3+} and PA-$AlCl_2^+$ complexes exhibit closer binding stability, providing further compelling evidence for the co-insertion of $AlCl_2^+$ and Al^{3+}.

3. Conclusion

In summary, we have developed an economically efficient, ultrafast, and stable Al-organic battery by simultaneously employing a molten salt electrolyte and incorporating strong π-π stacking interactions in the organic cathode design. The Al||PA450 molten salt battery exhibits remarkable electrochemical performance due to the rapid charge transfer kinetics and facile dissociation characteristics of the molten salt electrolyte, as well as the enhanced ion transport and material stability facilitated by strengthened π-π stacking interactions with PA450. The developed Al||PA450 organic molten salt battery significantly mitigates the potential polarization caused by high currents, thereby achieving high energy and power density for electrochemical energy storage and conversion under high-rate conditions. Even at an ultra-high current density of 10 A g^{-1}, PA450 exhibits a specific capacity of 110 mAh g^{-1} and an excellent cycling capability of up to 2000 cycles. In addition, by combining DFT calculations with experimental analysis, we have elucidated the multi-stage coupled energy storage characteristics based on $AlCl_2^+$ and Al^{3+} dual ions in the Al||PA450 molten salt battery. This distinguishes it from conventional Al-organic batteries, which rely primarily on monovalent $AlCl_2^+$ for redox reactions, leveraging the inherent advantage of multiple electron transfer in AlBs. This work presents a novel strategy for designing ultra-stable organic small-molecule cathode materials by developing and applying molten salt electrolytes. This innovation not only enhances the stability of the organic small-molecule but also promotes the advancement of cost-effective organic batteries suitable for large-scale energy storage.

CRediT authorship contribution statement

Xuanpeng Wang: Investigation. **Kang Han:** Writing – original draft, Investigation, Data curation. **Chaojiang Niu:** Investigation. **Zhenhang Zhong:** Investigation. **Liqiang Mai:** Writing – review & editing, Supervision, Funding acquisition. **Jiashen Meng:** Writing – review &

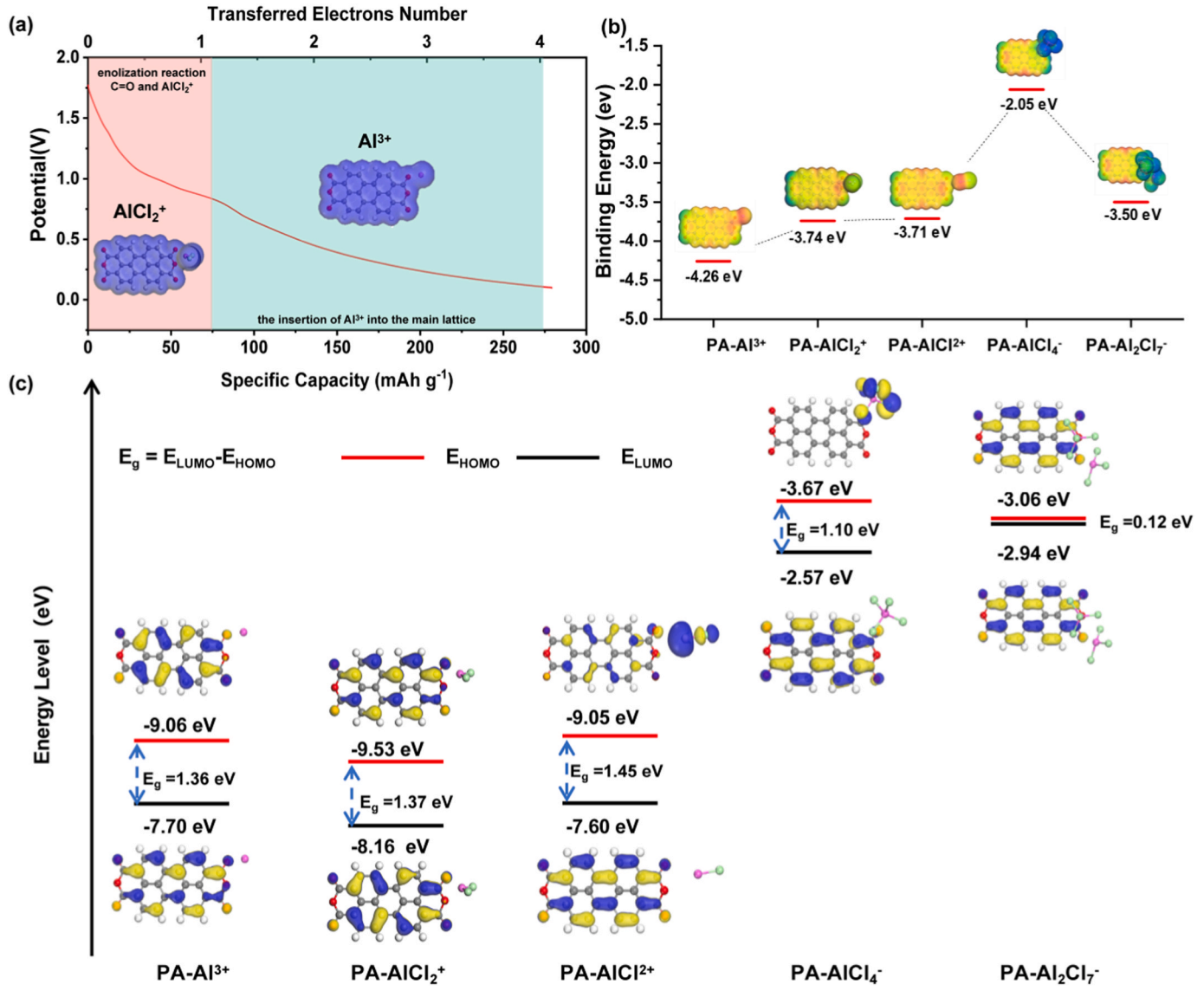

Fig. 5. Theoretical calculations for the analysis of potential energy storage mechanisms for PA450 (a) Galvanostatic voltage profiles and corresponding transferred electron numbers of PA450 at 1 A g^{-1}. (b,c) Theoretical calculation of binding energy (b) and HUMO, LUMO data (c)between PTCDA and different aluminum coordinating ions.

editing, Data curation. **Xinying Qiao:** Data curation. **Qi Zhang:** Investigation. **Meng Huang:** Supervision.

Declaration of Competing Interest

The authors declare that they have no known competing financial interests or personal relationships that could have appeared to influence the work reported in this paper.

Data availability

Data will be made available on request.

Acknowledgements

This work was supported by the National Key Research and Development Program of China (2020YFA0715000), National Energy-Saving and Low-Carbon Materials Production and Application Demonstration Platform Program (TC220H06N), National Natural Science Foundation of China (52127816).

Appendix A. Supporting information

Supplementary data associated with this article can be found in the online version at doi:10.1016/j.nanoen.2024.110085.

References

[1] J. Hu, Y. Hong, M. Guo, Y. Hu, W. Tang, S. Xu, S. Jia, B. Wei, S. Liu, C. Fan, Q. Zhang, Emerging organic electrodes for Na-ion and K-ion batteries, Energy Stor. Mater. 56 (2023) 267–299, https://doi.org/10.1016/j.ensm.2023.01.021.
[2] S. Lee, G. Kwon, K. Ku, K. Yoon, S.-K. Jung, H.-D. Lim, K. Kang, Recent progress in organic electrodes for Li and Na rechargeable batteries, Adv. Mater. 30 (2018) 1704682, https://doi.org/10.1002/adma.201704682.
[3] M. Sha, L. Liu, H. Zhao, Y. Lei, Review on Recent Advances of Cathode Materials for Potassium-ion Batteries, Energy Environ. Mater. 3 (2020) 56–66, https://doi.org/10.1002/eem2.12060.
[4] F. Xiong, Y. Jiang, L. Cheng, R. Yu, S. Tan, C. Tang, C. Zuo, Q. An, Y. Zhao, J.-J. Gaumet, L. Mai, Low-strain TiP_2O_7 with Three-dimensional Ion Channels as Long-life and High-rate Anode Material For Mg-ion batteries, Interdiscip. Mater. 1 (2022) 140–147, https://doi.org/10.1002/idm2.12004.
[5] F. Wu, H. Yang, Y. Bai, C. Wu, Paving the path toward reliable cathode materials for aluminum-ion batteries, Adv. Mater. 31 (2019) e1806510, https://doi.org/10.1002/adma.201806510.

[6] Y. Lu, J. Chen, Prospects of organic electrode materials for practical lithium batteries, Nat. Rev. Chem. 4 (2020) 127–142, https://doi.org/10.1038/s41570-020-0160-9.

[7] H. Wang, F. Liu, R. Yu, J. Wu, Unraveling the reaction mechanisms of electrode materials for sodium-ion and potassium-ion batteries by in situ transmission electron microscopy, Interdiscip. Mater. 1 (2022) 196–212, https://doi.org/10.1002/idm2.12008.

[8] D.J. Yoo, M. Heeney, F. Glocklhofer, J.W. Choi, Tetradiketone macrocycle for divalent aluminium ion batteries, Nat. Commun. 12 (2021) 2386, https://doi.org/10.1038/s41467-021-22633-y.

[9] Y. Hu, D. Sun, B. Luo, L. Wang, Recent progress and future trends of aluminum batteries, Energy Technol. 7 (2018) 86–106, https://doi.org/10.1002/ente.201800550.

[10] Z.Q. Hu, H. Zhang, H.Z. Wang, F.L. Zhang, Q. Li, H.S. Li, Nonaqueous aluminum ion batteries: recent progress and prospects, ACS Mater. Lett. 2 (2020) 887–904, https://doi.org/10.1021/acsmaterialslett.0c00208.

[11] H. Lahan, S.K. Das, An approach to improve the Al^{3+} ion intercalation in anatase TiO_2 nanoparticle for aqueous aluminum-ion battery, Ionics 24 (2018) 1855–1860, https://doi.org/10.1007/s11581-018-2530-6.

[12] Y. Lu, Q. Zhang, L. Li, Z. Niu, J. Chen, Design strategies toward enhancing the performance of organic electrode materials in metal-ion batteries, Chem 4 (2018) 2786–2813, https://doi.org/10.1016/j.chempr.2018.09.005.

[13] H. Yang, H. Li, J. Li, Z. Sun, K. He, H.-M. Cheng, F. Li, The rechargeable aluminum battery: opportunities and challenges, Angew. Chem. Int. Ed. Engl. 58 (2019) 11978–11996, https://doi.org/10.1002/anie.201814031.

[14] A.M. Diem, B. Fenk, J. Bill, Z. Burghard, Binder-free V_2O_5 cathode for high energy density rechargeable aluminum-ion batteries, Nanomaterials 10 (2020) 247, https://doi.org/10.3390/nano10020247.

[15] F. Guo, Z. Huang, M. Wang, W.-L. Song, A. Lv, X. Han, J. Tu, S. Jiao, Active cyano groups to coordinate $AlCl_2^+$ cation for rechargeable aluminum batteries, Energy Stor. Mater. 33 (2020) 250–257, https://doi.org/10.1016/j.ensm.2020.08.016.

[16] N. Zhu, F. Wu, Z.H. Wang, L.M. Ling, H.Y. Yang, Y.N. Gao, S.N. Guo, L.M. Suo, H. Li, H.J. Xu, Y. Bai, C. Wu, Reversible Al^{3+} storage mechanism in anatase TiO_2 cathode material for ionic liquid electrolyte-based aluminum-ion batteries, J. Energy Chem. 51 (2020) 72–80, https://doi.org/10.1016/j.jechem.2020.03.032.

[17] K.V. Kraychyk, S. Wang, L. Piveteau, M.V. Koyalenko, Efficient aluminum chloride natural graphite battery, Chem. Mater. 29 (2017) 4484–4492, https://doi.org/10.1021/acs.chemmater.7b01060.

[18] D.-Y. Wang, C.-Y. Wei, M.-C. Lin, C.-J. Pan, H.-L. Chou, H.-A. Chen, M. Gong, Y. Wu, C. Yuan, M. Angell, Y.-J. Hsieh, Y.-H. Chen, C.-Y. Wen, C.-W. Chen, B.-J. Hwang, C.-C. Chen, H. Dai, Advanced rechargeable aluminium ion battery with a high-quality natural graphite cathode, Nat. Commun. 8 (2017) 14283, https://doi.org/10.1038/ncomms14283.

[19] H.P. Lei, M.Y. Wang, J.G. Tu, S. Jiao, Single-crystal and Hierarchical VSe_2 as an Aluminum-Ion Battery Cathode, Sustain Energ. Fuels 3 (2019) 2717–2724, https://doi.org/10.1039/c9se00288j.

[20] G. Li, J. Tu, M. Wang, S. Jiao, Cu_3P as a novel cathode material for rechargeable aluminum-ion batteries, J. Mater. Chem. A 7 (2019) 8368–8375, https://doi.org/10.1039/c9ta00762h.

[21] H. Li, H. Yang, Z. Sun, Y. Shi, H.-M. Cheng, F. Li, A highly reversible Co_3S_4 microsphere cathode material for aluminum-ion batteries, Nano Energy 56 (2019) 100–108, https://doi.org/10.1016/j.nanoen.2018.11.045.

[22] J. Liu, Z. Li, X. Huo, J. Li, Nanosphere-rod-Like Co_3O_4 as high performance cathode material for aluminium ion batteries, J. Power Sources 422 (2019) 49–56, https://doi.org/10.1016/j.jpowsour.2019.03.029.

[23] Y. Zhang, S. Liu, Y. Ji, J. Ma, H. Yu, Emerging nonaqueous aluminum-ion batteries: challenges, status, and perspectives, Adv. Mater. 30 (2018) e1706310, https://doi.org/10.1002/adma.201706310.

[24] H. Yang, L. Yin, J. Liang, Z. Sun, Y. Wang, H. Li, K. He, L. Ma, Z. Peng, S. Qiu, C. Sun, H.-M. Cheng, F. Li, An aluminum–sulfur battery with a fast kinetic response, Angew. Chem. Int. Ed. Engl. 57 (2018) 1898–1902, https://doi.org/10.1002/anie.201711328.

[25] M. Walter, K.V. Kravchyk, C. Böfer, R. Widmer, M.V. Kovalenko, Polypyrenes as high-performance cathode materials for aluminum batteries, Adv. Mater. 30 (2018) 1705644, https://doi.org/10.1002/adma.201705644.

[26] X. Yu, B. Wang, D. Gong, Z. Xu, B. Lu, Graphene nanoribbons on highly porous 3D graphene for high-capacity and ultrastable Al-ion batteries, Adv. Mater. 29 (2017) 1604118, https://doi.org/10.1002/adma.201604118.

[27] Y. Hu, D. Ye, B. Luo, H. Hu, X. Zhu, S. Wang, L. Li, S. Peng, L. Wang, A binder-free and free-standing cobalt sulfide@ carbon nanotube cathode material for aluminum-ion batteries, Adv. Mater. 30 (2018) 1703824, https://doi.org/10.1002/adma.201703824.

[28] K. Liang, L. Ju, S. Koul, A. Kushima, Y. Yang, Self-supported tin sulfide porous films for flexible aluminum-ion batteries, Adv. Energy Mater. 9 (2019) 1802543, https://doi.org/10.1002/aenm.201802543.

[29] T. Cai, L. Zhao, H. Hu, T. Li, X. Li, S. Guo, Y. Li, Q. Xue, W. Xing, Z. Yan, Stable $CoSe_2$/carbon nanodice@reduced graphene oxide composites for high-performance rechargeable aluminum-ion batteries, Energy Environ. Sci. 11 (2018) 2341–2347, https://doi.org/10.1039/C8EE00822A.

[30] J. Jiang, H. Li, T. Fu, B.-J. Hwang, X. Li, J. Zhao, One-dimensional $Cu_{2-x}Se$ nanorods as the cathode material for high-performance aluminum-ion battery, ACS Appl. Mater. Interfaces 10 (2018) 17942–17949, https://doi.org/10.1021/acsami.8b03259.

[31] M.-C. Lin, M. Gong, B. Lu, Y. Wu, D.-Y. Wang, M. Guan, M. Angell, C. Chen, J. Yang, B.-J. Hwang, H. Dai, An ultrafast rechargeable aluminium-ion battery, Nature 520 (2015) 324–328, https://doi.org/10.1038/nature14340.

[32] R. Precht, R. Hausbrand, W. Jaegermann, Electronic structure and electrode properties of tetracyanoquinodimethane (TCNQ): a surface science investigation of lithium intercalation into TCNQ, Phys. Chem. Chem. Phys. 17 (2015) 6588–6596, https://doi.org/10.1039/c4cp05206d.

[33] N. Canever, T. Nann, Unraveling the multivalent aluminium-ion redox mechanism in 3,4,9,10-perylenetetracarboxylic dianhydride (PTCDA), Phys. Chem. Chem. Phys. 24 (2022) 5886–5893, https://doi.org/10.1039/d1cp05716b.

[34] S. Wang, S. Huang, M. Yao, Y. Zhang, Z. Niu, Engineering active sites of polyaniline for $AlCl_2^+$ storage in an aluminum-ion battery, Angew. Chem. Int. Ed. Engl. 59 (2020) 11800–11807, https://doi.org/10.1002/anie.202002132.

[35] Y. Liu, Y. Lu, A. Hossain Khan, G. Wang, Y. Wang, A. Morag, Z. Wang, G. Chen, S. Huang, N. Chandrasekhar, D. Sabaghi, D. Li, P. Zhang, D. Ma, E. Brunner, M. Yu, X. Feng, Redox-bipolar polyimide two-dimensional covalent organic framework cathodes for durable aluminium batteries, Angew. Chem. Int. Ed. Engl. 62 (2023) e202306091, https://doi.org/10.1002/anie.202306091.

[36] S. Li, Y. Liu, L. Dai, S. Li, B. Wang, J. Xie, P. Li, A stable covalent organic framework cathode enables ultra-long cycle life for alkali and multivalent metal rechargeable batteries, Energy Stor. Mater. 48 (2022) 439–446, https://doi.org/10.1016/j.ensm.2022.03.033.

[37] J. Zhang, Y. Wu, M. Liu, L. Huang, Y. Li, Y. Wu, Self-adaptive Re-organization enables polythiophene as an extraordinary cathode material for aluminum-ion batteries with a cycle life of 100 000 cycles, Angew. Chem. 135 (2023) e202215408, https://doi.org/10.1002/anie.202215408.

[38] X. Peng, Y. Xie, A. Baktash, J. Tang, T. Lin, X. Huang, Y. Hu, Z. Jia, D.J. Searles, Y. Yamauchi, L. Wang, B. Luo, Heterocyclic conjugated polymer nanoarchitectonics with synergistic redox-active sites for high-performance aluminium organic batteries, Angew. Chem. Int. Ed. Engl. 61 (2022) e202203646, https://doi.org/10.1002/anie.202203646.

[39] Q. Pang, J. Meng, S. Gupta, X. Hong, C.Y. Kwok, J. Zhao, Y. Jin, L. Xu, O. Karahan, Z. Wang, S. Toll, L. Mai, L.F. Nazar, M. Balasubramanian, B. Narayanan, D. R. Sadoway, Fast-charging aluminium-chalcogen batteries resistant to dendritic shorting, Nature 608 (2022) 704–711, https://doi.org/10.1038/s41586-022-04983-9.

[40] Y. Huang, R. Yuan, S. Zhou, Gas phase-based growth of highly sensitive single-crystal rectangular micro-and nanotubes, J. Mater. Chem. 22 (2012) 883–888, https://doi.org/10.1039/c1jm14238k.

[41] T. Ogawa, K. Kuwamoto, S. Isoda, T. Kobayashi, N. Karl, 3, 4: 9, 10-Perylenete-tracarboxylic dianhydride (PTCDA) by electron crystallography, Acta Crystallogr. B 55 (1999) 123–130, https://doi.org/10.1107/s0108768198009872.

[42] H. Zhang, Y. Fang, F. Yang, X. Liu, X. Lu, Aromatic organic molecular crystal with enhanced π–π stacking interaction for ultrafast Zn-ion storage, Energy Environ. Sci. 13 (2020) 2515–2523, https://doi.org/10.1039/D0EE01723J.

[43] Y. Huang, Y. Yan, B.M. Smarsly, Z. Wei, C.F.J. Faul, Helical supramolecular aggregates, mesoscopic organisation and nanofibers of a perylenebisimide–chiral surfactant complex via ionic self-assembly, J. Mater. Chem. 19 (2009) 2356–2362, https://doi.org/10.1039/B817838K.

[44] L. Fan, R. Ma, J. Wang, H. Yang, B. Lu, An ultrafast and highly stable potassium-organic battery, Adv. Mater. 30 (2018) e1805486, https://doi.org/10.1002/adma.201805486.

[45] G. Ou, Z. Song, W. Gui, F. Zhang, Surface and interface analysis of PTCDA/ITO using X-ray photoelectron spectroscopy (XPS), Guang Pu Xue Yu Guang Pu Fen. Xi 26 (2006) 753–756.

[46] S.W. Cho, D. Newby, Jr, A. DeMasi, K.E. Smith, L.F. Piper, T.S. Jones, Determination of the individual atomic site contribution to the electronic structure of 3,4,9,10-perylene-tetracarboxylic-dianhydride (PTCDA), J. Chem. Phys. 139 (2013) 184711, https://doi.org/10.1063/1.4829764.

[47] T. Lu, Q. Chen, A simple method of identifying π orbitals for non-planar systems and a protocol of studying π electronic structure, Theor. Chem. Acc. 139 (2020) 25, https://doi.org/10.1007/s00214-019-2541-z.

[48] E.R. Johnson, S. Keinan, P. Mori-Sánchez, J. Contreras-García, A.J. Cohen, W. Yang, Revealing noncovalent interactions, J. Am. Chem. Soc. 132 (2010) 6498–6506, https://doi.org/10.1021/ja100936w.

[49] T. LU, F.-W. CHEN, , Meaning and functional form of the electron localization function, Acta Phys. Chim. Sin. 27 (2011) 2786–2792, https://doi.org/10.3866/PKU.WHXB20112786.

[50] Y. Liu, W. Luo, S. Lu, Z. Zhang, Z. Chao, J. Fan, Novel carbonyl cathode for green and sustainable aluminum organic batteries, ACS Appl. Mater. Interfaces 14 (2022) 53702–53710, https://doi.org/10.1021/acsami.2c14365.

[51] D. Kong, T. Cai, H. Fan, H. Hu, X. Wang, Y. Cui, D. Wang, Y. Wang, H. Hu, M. Wu, Q. Xue, Z. Yan, X. Li, L. Zhao, W. Xing, Polycyclic aromatic hydrocarbons as a new class of promising cathode materials for aluminum-ion batteries, Angew. Chem. Int. Ed. Engl. 61 (2022) e202114681, https://doi.org/10.1002/anie.202114681.

[52] D.J. Kim, D.-J. Yoo, M.T. Otley, A. Prokofjevs, C. Pezzato, M. Owczarek, S.J. Lee, J. W. Choi, J.F. Stoddart, Rechargeable aluminium organic batteries, Nat. Energy 4 (2019) 51–59, https://doi.org/10.1038/s41560-018-0291-0.

[53] X. Han, S. Li, W.-L. Song, N. Chen, H. Chen, S. Huang, S. Jiao, Stable high-capacity organic aluminum–porphyrin batteries, Adv. Energy Mater. 11 (2021) 2101446, https://doi.org/10.1002/aenm.202101446.

[54] J. Kim, M.R. Raj, G. Lee, High-defect-density graphite for superior-performance aluminum-ion batteries with ultra-fast charging and stable long life, Nano-Micro Lett. 13 (2021) 171, https://doi.org/10.1007/s40820-021-00698-0.

[55] Y. Guo, W. Wang, H. Lei, M. Wang, S. Jiao, Alternate storage of opposite charges in multisites for high-energy-density Al–MOF batteries, Adv. Mater. 34 (2022) 2110109, https://doi.org/10.1002/adma.202110109.
[56] A. Eilmes, P. Kubisiak, P. Wróbel, Explicit and Hybrid Solvent Models for Estimates of Parameters Relevant to the Reduction Potential of Ethylene Carbonate, International Journal of Molecular Sciences 23 (2022) 15590, https://doi.org/10.3390/ijms232415590.
[57] J.-i Aihara, Reduced HOMO−LUMO gap as an index of kinetic stability for polycyclic aromatic hydrocarbons, J. Phys. Chem. A 103 (1999) 7487–7495, https://doi.org/10.1021/jp990092i.